Journal of Computational Acoustics, Vol. 9, No. 3 (2001) 1203–1214
© IMACS

THREE-DIMENSIONAL GROUND MOTION SIMULATIONS FOR LARGE EARTHQUAKES ON THE SAN ANDREAS FAULT WITH DYNAMIC AND OBSERVATIONAL CONSTRAINTS*

KIM B. OLSEN

Institute for Crustal Studies UCSB, Santa Barbara, CA 93016-1100, USA

Received 4 October 1999
Revised 4 September 2000

I have simulated 0–0.5 Hz viscoelastic ground motion in Los Angeles from M 7.5 earthquakes on the San Andreas fault using a fourth-order staggered-grid finite-difference method. Two scenarios are considered: (a) a southeast propagating and (b) a northwest propagating rupture along a 170-km long stretch of the fault near Los Angeles in a 3D velocity model. The scenarios use variable slip and rise time distributions inferred from the kinematic inversion results for the 1992 M 7.3 Landers, California, earthquake. The spatially variable static slip distribution used in this study, unlike that modeled in a recent study,[1] is in agreement with constraints provided by rupture dynamics. I find peak ground velocities for (a) and (b) of 49 cm/s and 67 cm/s, respectively, near the fault. The near-fault peak motions for scenario (a) are smaller compared to previous estimates from 3D modeling for both rough and smooth faults.[1,2] The lower near-fault peak motions are in closer agreements with constraints from precarious rocks located near the fault. Peak velocities in Los Angeles are about 30% larger for (b) 45 cm/s compared to those for (a) 35 cm/s.

1. Introduction

One of the greatest hazards in southern California is a large earthquake on the stretch of the San Andreas fault (SAF) located near Los Angeles (LA). This part of the SAF which consists of two segments, the Mojave and part of the San Bernardino Mtns. segment,[3] is believed to have produced the M 7.5 earthquake on 12 Dec. 1812.[3] The average recurrence time for large earthquakes with surface rupture is 150^{+123}_{-71} yrs on the Mojave segment and 146^{+91}_{-60} yrs on the San Bernardino segment.[3] The Working Group on California Earthquake Probabilities (WGCEP), 1995, estimated mean conditional probabilities of $26 \pm 11\%$ (M 7.53) and $28 \pm 13\%$ (M 7.30) for events on the Mojave and San Bernardino segments, respectively, to occur before the year 2024.[3]

Two earlier studies[1,2] have presented wave propagation from large earthquakes on the SAF and their resulting ground motion in the LA region. Both studies considered a southeast propagating rupture along a 170 km stretch of the SAF from Tejon Pass to San Bernardino. The early study[2] used a simplified rupture scenario with smooth slip and constant rise time.

*Presented at ICTCA'99, the 4th International Conference on Theoretical and Computational Acoustics, May 1999, Trieste, Italy.

The study found 0–0.4 Hz peak velocities near the fault and in LA of 2.5 m/s and 1.4 m/s, respectively for a M 7.75 scenario. The more recent study[1] found that variable slip and rise time distributions tend to reduce the ground motion estimates. Both studies found that the 3D basin structure significantly amplifies the ground motions and extends the durations, in part due to surface waves generated at the basin edges.

While the recent rupture scenario[1] went beyond the simplifications of constant slip and rise time, their rupture scenario is in disagreement with constraints derived from rupture dynamics. Their rough asperity model, derived by combining slip distributions obtained from kinematic slip inversions of the 1992 Landers earthquake, contains an approximately 30 km long stretch in the center of the fault with slip only in two small, unconnected asperities. The results from 3D dynamic rupture modeling of the 1992 Landers earthquake[4] have shown that the generation of rupture propagation with radiation in agreement with observations required an initial stress distribution with a high connectivity between the individual asperities. In order for the scenario to propagate through the entire fault in the recently published rough asperity model[1] it would be necessary for the rupture to jump. However, studies of dynamic rupture propagation in the presence of fault segmentation[5,6] show little evidence of rupture between segments located more than about five km apart.

The two previous studies of wave propagation from large earthquakes on the SAF only considered ruptures propagating toward the southeast. However, the direction of propagation for future earthquakes on the SAF is unknown. In order to analyze the effects of the direction of rupture propagation on the ground motion in LA I compute ground motions for two scenarios: (a) rupture towards the southeast (SAFN) and (b) rupture towards the northwest (SAFS). I use a fourth-order viscoelastic finite-difference method and a slip distribution derived from kinematic studies of the 1992 Landers earthquake, which unlike that used in the recent study,[1] is in agreement with constraints derived from dynamic rupture modeling. I use a six time window slip distribution,[7] similar to that used in the previous rough asperity model.[1] The slip and slip rate distributions used in my modeling is thus in agreement with results from both kinematic inversion and dynamic modeling. I also extend the ground motion estimates to slightly higher frequencies (0.5 Hz) compared to the previous studies (0.4 Hz).

Recently, a constraint has been posed for the upper level of ground motions near the SAF by estimating the peak motions required to topple nearby precarious rocks.[8] Both of the earlier reported near-fault peak motions[1,2] are larger than the values estimated as necessary to topple the precarious rocks, if the higher frequencies are estimated using the reponse spectrum shape corresponding to the USGS-CDMG hazard curves[9] (Brune, Personal Communication, 1998). Here, I investigate whether a more realistic slip distribution can bring the near-fault peak motions in better agreement with the constraints from the study of precarious rocks.

This paper is divided into the following parts. After the introduction, the LA basin model and earthquake scenarios are described. The following section describes the finite-difference scheme and the finite-fault source implementation used in the simulations. The LA basin peak velocities are then presented and I discuss the wave propagation using synthetic seismograms and snapshots.

2. Description of the Earth Model and Scenario Earthquakes

I use the Southern California Earthquake Center (SCEC) 3D velocity model version 1 of the LA area.[10] Outside the 3D basin structures the model is a 1D regional model.[11] The spatial resolution of the model is approximately 0.5 km (H. Magistrale, written communication, 1995). Within the basins the P-wave velocity is determined from the depths and ages estimated for four geological horizons[12] and calibrated with local P-wave velocity models for the basins. The density is estimated from the P-wave velocity using the Nafe-Drake relation.[13] Then the density is used to find Poisson's ratio.[14] Finally, the S-wave velocity is computed from the P-wave velocity and Poisson's ratio.

Figure 1 shows a topographic map of southern California. The rectangular area depicts the extent of the model for the SAF scenarios. The 3D nature of the model is characterized in Fig. 2 by the isosurface corresponding to an S-wave velocity of 2.5 km/s. The large depression is the LA basin. The smaller basin to the northwest is located below the San Fernando Valley (SFV), separated from the LA basin by the Santa Monica Mountains, with the Ventura basin continuing to the North. A relatively small basin is located below the San Gabriel Valley (SGV), and the larger, but shallower Chino basin extends the LA basin to the East. Finally, the San Bernardino basin continues the Chino basin eastward to the SAF. Note that the reference frame of the model in Fig. 2 is rotated 28° counterclockwise from North to minimize the computational requirements for the simulations. The axis of the main basin trends approximately 118° as does the SAF. Throughout this paper I use azimuths of

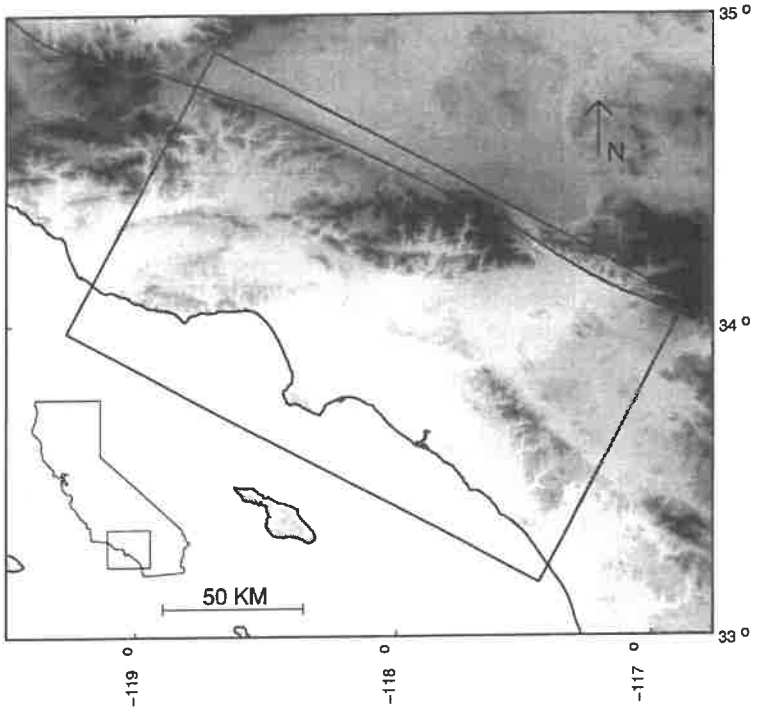


Fig. 1. Topographic map of southern California centered on the Los Angeles region, showing the modeling area (rectangle), and the trace of the SAF.

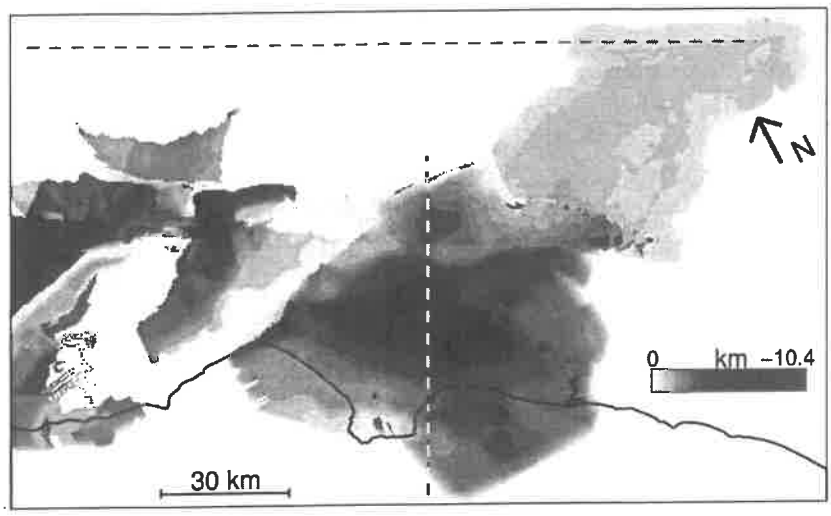


Fig. 2. 3D image of the isosurface for an S-wave velocity of 2.5 km/s for the area within the rectangle shown in Fig. 1. The northwest-southeast trending line depicts the 170-km long stretch of the SAF along which I simulated rupture. The northeast-southwest trending line is a profile used to display synthetic seismograms.

118° and 28° to analyze the horizontal ground motion for the earthquake simulations. The topography above sea level is not included in the simulations.

3. Finite Difference Modeling

I use a staggered-grid velocity-stress finite-difference method, with fourth-order spatial and second-order temporal accuracy.[15,2,16,17,18] The source is implemented in the finite-difference grid by adding $-M_{ij}(t)/V$ to $S_{ij}(t)$ where $M_{ij}(t)$ is the ijth component of the moment tensor for the earthquake, V = dx^3 is the cell volume, and $S_{ij}(t)$ is the ijth component of the stress tensor on the fault at time t. The synthetic seismograms are lowpass filtered to frequencies less than 0.5 Hz (Butterworth filter with four poles and two passes).

Finite-difference simulations include a trade-off between the highest frequency and smallest velocity in the models. Although near-surface sediments have lower velocities, I have imposed a minimum S-wave velocity of 1 km/s in my model. The physical model is discretized with a grid spacing of 0.4 km ($\approx$ 20 million nodes) equivalent to five nodes per minimum shear wavelength of 2.5 km, the rule-of-thumb commonly used for fourth-order schemes[19] which here limits the maximum resolved frequency to 0.5 Hz. Absorbing boundary conditions[20] are applied to the sides of the computational model. To further reduce artificial reflections the boundaries of the model are padded with a zone of attenuative material.[21]

Viscoelasticity is implemented using stress relaxation independently for P and S waves[22,23] using a standard linear solid model with one relaxation peak. The accuracy of the smallest Q in the model, $Q_s = 100$, is estimated to less than about 5% for the central 1/3 of the bandwidth of interest.[22] There are essentially no constraints on the values of Q for the area of interest, and no well-established relation between Q and velocity is available.

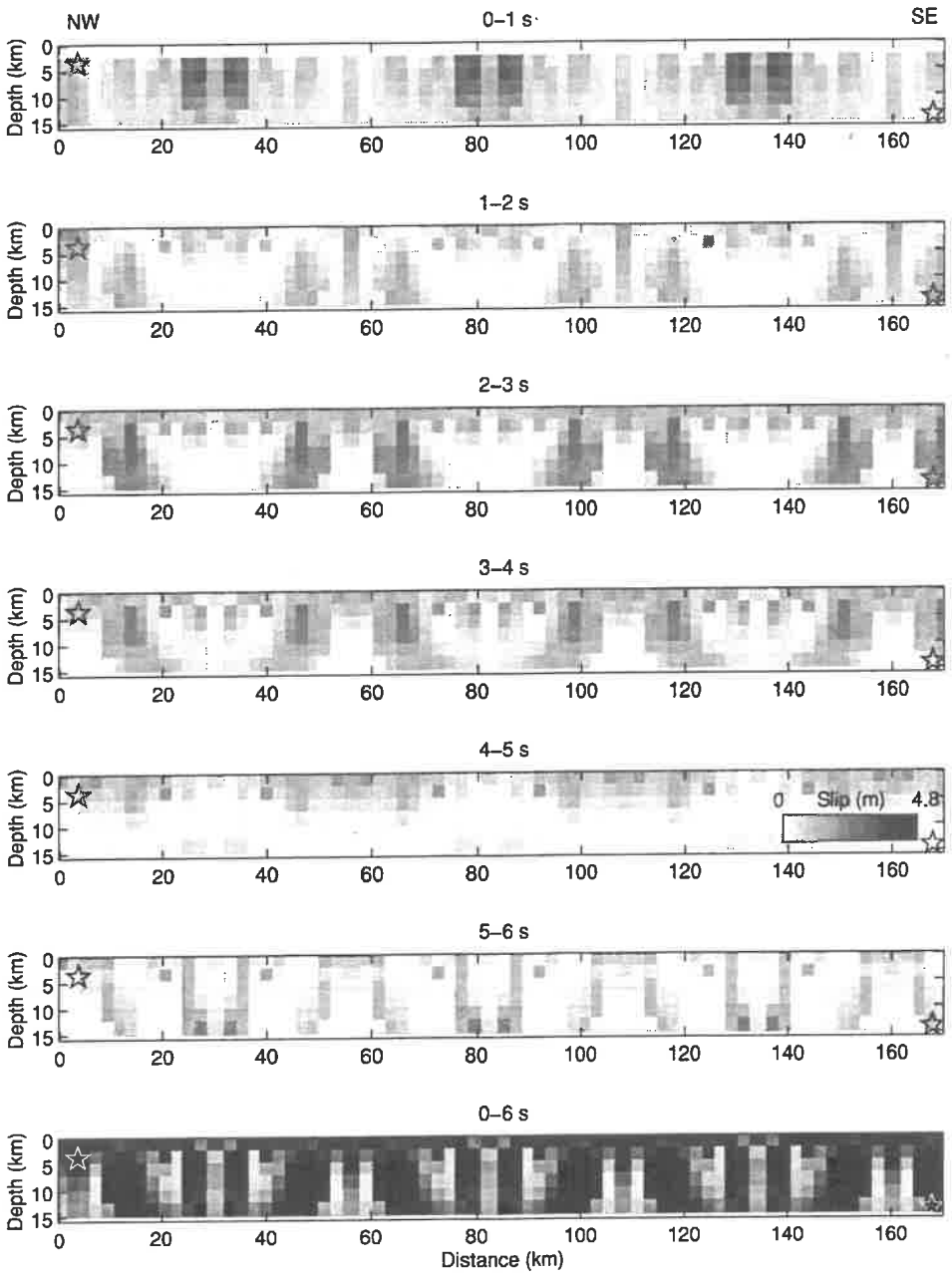


Fig. 3. Variable slip distributions for the two earthquake scenarios. The stars depict the hypocenters in the simulations.

I assumed that Q_s=0.1 Vs (km/s) and $Q_p = 1.5\ Q_s$ which, to my knowledge, is commonly used in absence of better constraints on Q.

The scenario rupture parameters are listed in Table 1, and the 3D modeling parameters are listed in Table 2. The slip and rise time distributions (Fig. 3) are taken as the six

Table 1. Earthquake Rupture Parameters.

	Hypocenter Longitude, Latitude, Depth (km)	Fault Width, Length, Depth to Top (km)	Dip	Strike	Rake	Moment Magnitude
SAFN	−118.657, 34.79, 4.0	16, 170, 0.4	90	118	180	7.5
SAFS	−117.088, 34.095, 15.2	16, 170, 0.4	90	118	180	7.5

Table 2. 3-D Modeling Parameters.

Spatial discretization (km)	0.4
Temporal discretization (sec)	0.025
Lowest P-wave velocity (km/sec)	2.41
Lowest S-wave velocity (km/sec)	1.0
Lowest Density (kg/m^3)	2070
Number of timesteps	5000
Simulation time (sec)	125

time window kinematic inversion results for the 1992 Landers[7] event, repeated several times along the fault. The source is added using six isosceles triangular sliprate time functions without overlap, as in the kinematic study.[7] Note that I have maintained a highly connected distribution of slip, as dictated by dynamic modeling results[4,24] for rupture to propagate. The scenarios use a rupture velocity of 85% of the local shear-wave velocity.

4. Numerical Results

Figure 4 shows peak velocity distributions for the two scenarios described above. Peak velocities for SAFN and SAFS are 49 cm/s and 67 cm/s, respectively, in the vicinity of the fault. The near-fault peak velocities for SAFN are generally lower than those obtained in the recent estimate.[1] Reasons for the smaller peak motions include a slip distribution with higher connectivity and a smaller maximum slip of 4.8 m used in this study compared to 9.7 m.[1] The lower near-fault peak motions obtained here are in better agreement with constraints from precarious rocks located near the fault.[8]

My simulations show that both the pattern and amplitudes vary considerably in the LA basin areas. While the deeper basin areas are generally characterized by increased peak velocities, some of the largest values tend to occur above the most steeply-dipping basin boundaries and the basin edges, in agreement with other results for the LA basin[16,17] and the Salt Lake Basin.[25] Note that the amplification varies significantly for the two scenarios. For example, the largest amplification due to the SAFN occurs in the southern end of the basin, while that for the SAFS occurs in the western parts. This pattern is due to reflections from the basin boundaries and surface wave generation at the edges. Peak velocities in LA are about 30% larger for (b) 45 cm/s compared to those for (a) 35 cm/s. In particular, the

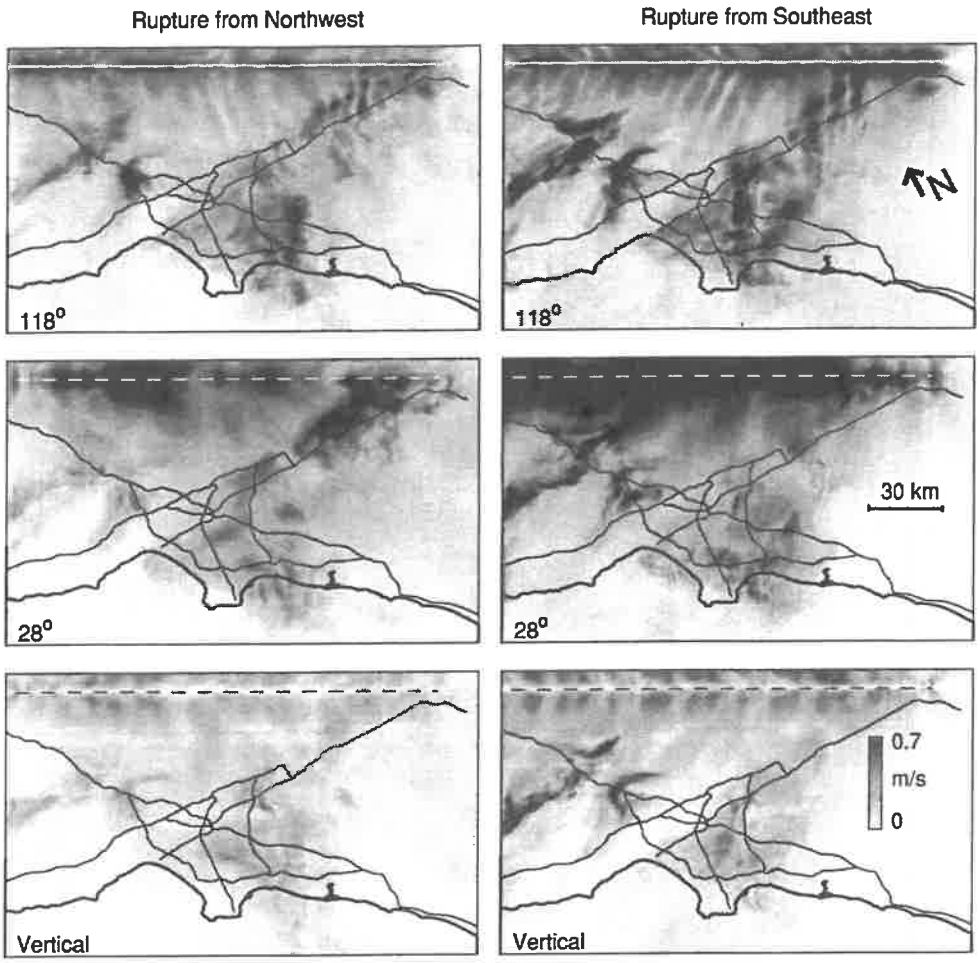


Fig. 4. Maps of 3D 0–0.5 Hz peak velocities for the two scenarios (see Figs. 1 and 2). The thin lines show major freeways in the Los Angeles area.

vertical peak velocities differ between the SAFN (17 cm/s) and SAFS (40 cm/s) scenarios. These results show that the variation in the 3D response is in part controlled by the azimuth of the incident waves, in agreement with recent findings for other scenarios.[17]

Figure 5 shows synthetic seismograms along the profile in Fig. 2 for the two scenarios. The profile is selected to intersect the deepest part of the LA basin, and it is located above some of the sites representing the largest amplification in the model area (see Fig. 4). In particular, the profile is located near the peaks in amplification obtained in the San Gabriel Valley and the main trough of the LA basin. The synthetics are scaled by the same factor for all components for both scenarios. The distance measures used in the following discussion refer to those shown in Fig. 5. The strike-slip SAF scenarios generate predominantly SH energy, with the 28° component amplified near the fault due to directivity effects.[2] The much extended duration that the scenarios generate along the profile is due not only to basin effects, but also to the rupture duration in excess of 60 s. A Love wave with southerly

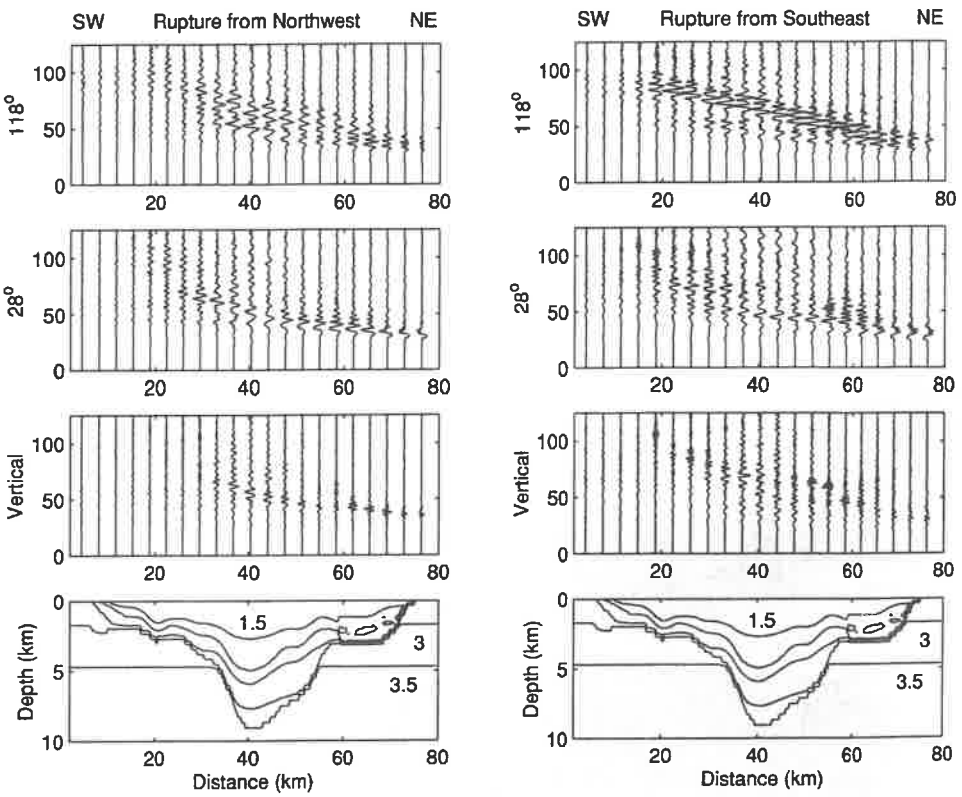


Fig. 5. Synthetic seismograms for the two scenarios along the profile shown in Fig. 2. The traces are scaled by the same factor for all components and both scenarios. The bottom panels show cross sections of the 3D models along the profile. Contours (some labeled) vary between 1.5 km/s and 3.5 km/s with a spacing of 0.5 km/s.

propagation direction and particularly strong dispersion for SAFS is generated when the wavefield enters the SGV, causing increased amplification at 55–70 km on the 28° component. Resonance is generated in the LA basin between at 40–60 km (see also snapshots in Figs. 6 and 7, 50 s and later), where the particle motion differs from that of a Rayleigh wave.

The amplification of the wavefield for SAFS is generally stronger than that for SAFN in the basin areas. A major reason for this pattern is the direction of the rupture propagation relative to the basin geometry. For example, the relatively stronger motions in the San Fernando Valley and eastern Ventura basin for SAFS compared to that for SAFN is to a large extent due to directivity effects of the wavefield upon entering these areas. In addition, the wavefield for SAFS is amplified relatively more along the boundary between the SAF and the San Bernardino basin. Finally, the wavefield for SAFS, in particular on the fault-parallel component, experiences larger amplification in the LA basin due to a stronger refraction and focusing upon entering the San Gabriel Valley (see snapshots at 37.5 s–62.5 s in Fig. 7). Further discussion of the amplification patterns for the SAF scenarios as well seven other scenarios can be found in the Phase 3 report from the Southern California Earthquake Center (SCEC).[17]

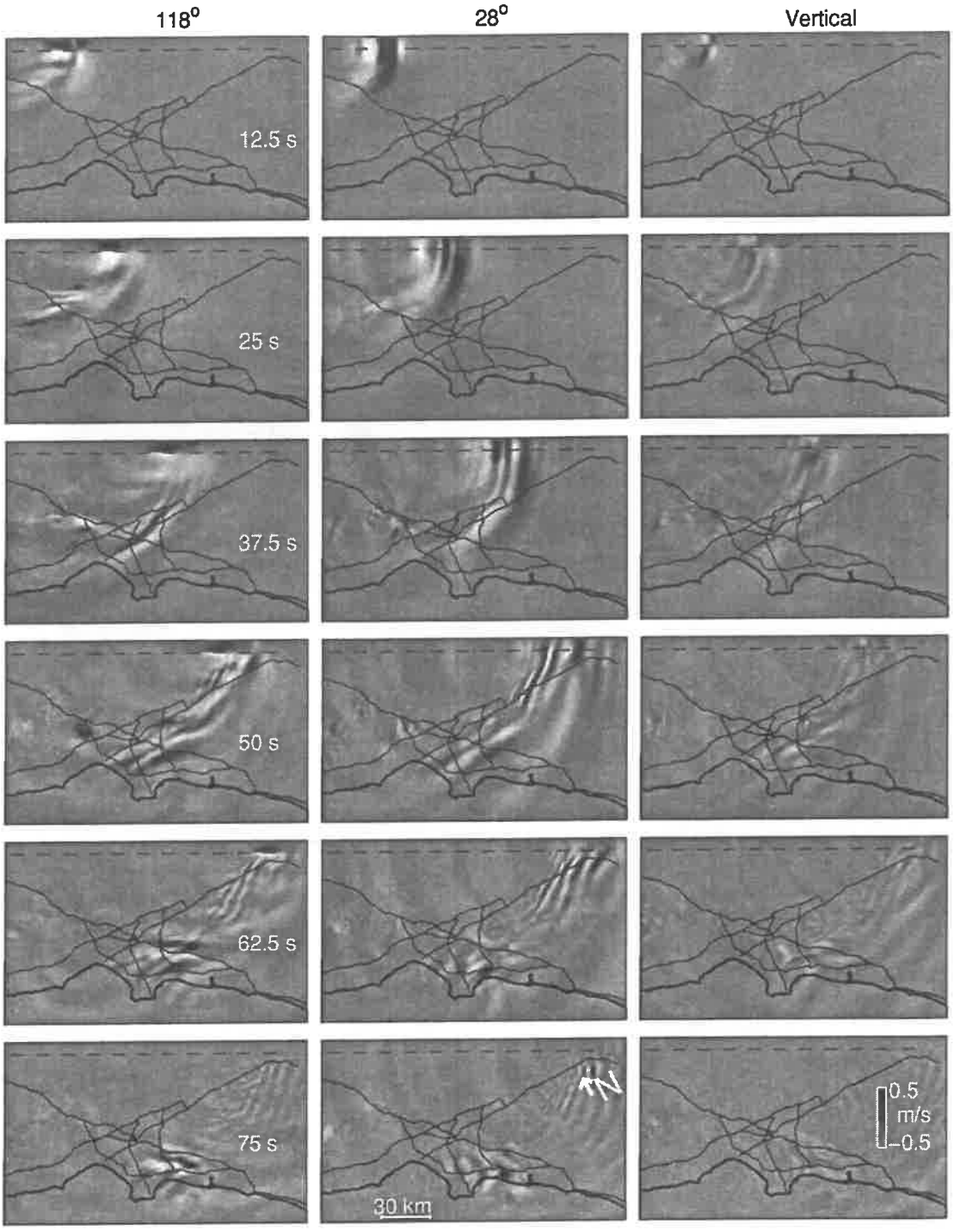


Fig. 6. Snapshots of simulated wave propagation in the Los Angeles area for SAFN along 118°, 28°, and vertical from 6.25 to 75 s after the origin time of the rupture. Light (dark) shading depicts negative (positive) particle velocity. The particle motion is scaled by a constant for all snapshots. The straight line depicts the surface fault trace. The thin lines show major freeways.

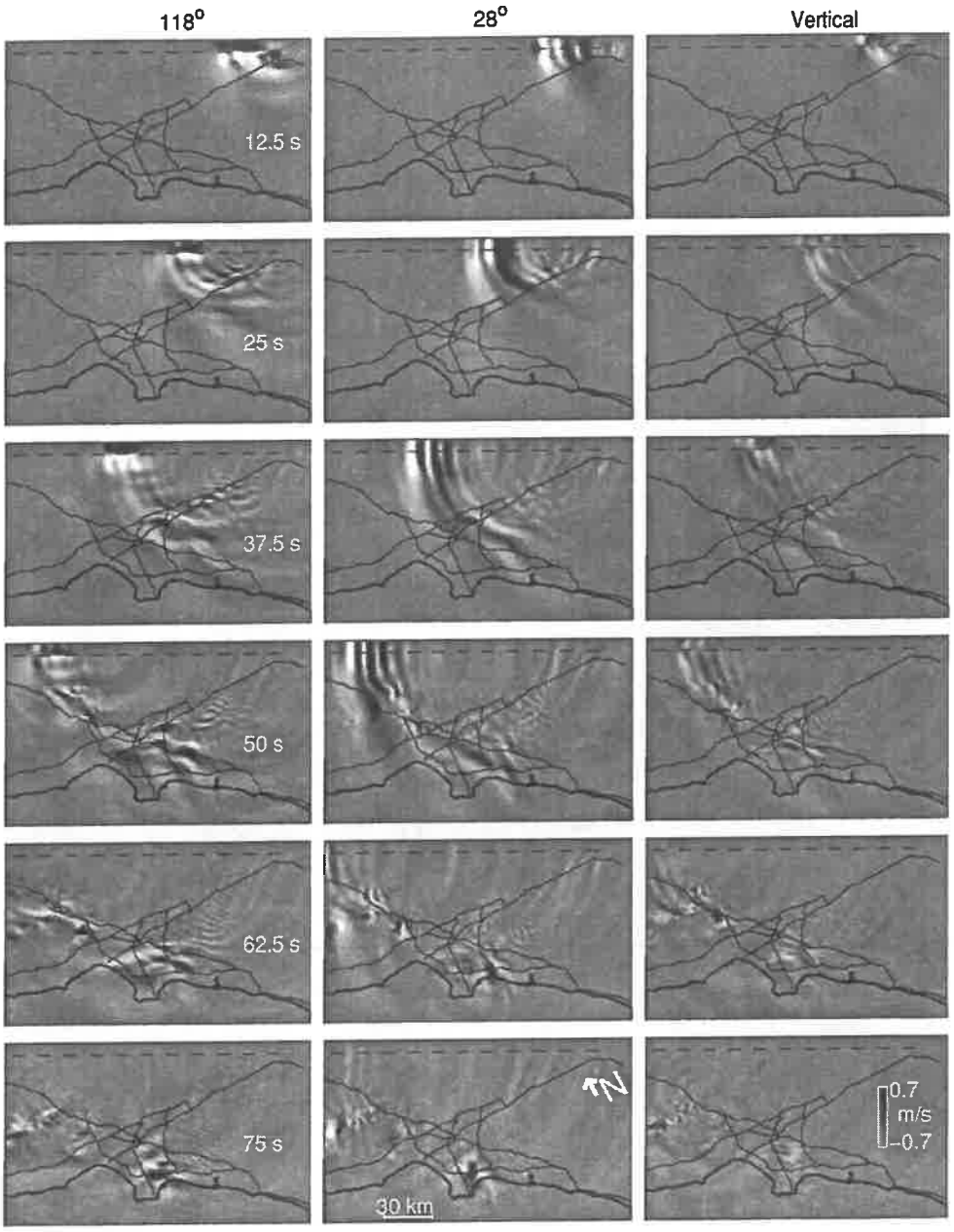


Fig. 7. Same as Fig. 6, but for SAFS.

5. Discussion and Conclusions

I have simulated 3D 0–0.5 Hz wave propagation for two large earthquake scenarios on the San Andreas fault. The pattern and amplitudes of the peak velocity distributions depend considerably on the direction of the rupture propagation. The peak velocities near the fault are up to 67 cm/s for the rupture starting at the northwestern end of the fault, compared

to 49 cm/s for the rupture starting at the southeastern end of the fault. These values are generally smaller than those estimated by previous 3D finite-difference simulations of ground motion for the scenario propagating southeast. Reasons for the smaller near-fault peak motions obtained in this study include a slip distribution with higher connectivity and smaller maximum slip. The near-fault peak motions are in closer agreement with constraints from threshold ground motions required to topple precarious rocks near the SAF. The peak velocities above the Los Angeles basin are largest for the scenario with rupture propagation toward northwest (45 cm/s), compared to those for the scenario with rupture propagation toward southeast (35 cm/s). In addition, the former rupture generates vertical peak velocities (40 cm/s) of more than twice the value of those for the latter (17 cm/s) in the Los Angeles basin due to resonances, controlled in part by the azimuth of the incident wavefield. The largest peak velocities occur in part above the deepest parts of the basin, in part above the steeply-dipping basin boundaries.

I realize that the minimum velocity of 1 km/s used in the simulations is unrealistically high for the basin sediments. In fact, the isosurface for $V_s = 1$ km/s extends to a maximum depth of 1.3 km in the center of the LA basin. However, it is presently not feasible to include considerably lower velocities in the simulations with a maximum resolved frequency of 0.5 Hz. I therefore leave this important task for future work.

Acknowledgements

The computations in this study were carried out on the SGI Origin 2000 at University of California, Santa Barbara (NSF grant CDA96-01954). This research was supported by the Southern California Earthquake Center. SCEC is funded by NSF Cooperative Agreement EAR-8920136 and USGS Cooperative Agreements 14-08-0001-A0899 and 1434-HQ-97AG01718. The SCEC contribution number for this paper is 530 and the Institute for Crustal Studies contribution number is 375-113EQ.

References

1. R. W. Graves, "Three-dimensional finite-difference modeling of the San Andreas fault: source parameterization and ground motion levels," *Bull. Seism. Soc. Am.* **88**, 881 (1998).
2. K. B. Olsen, R. J. Archuleta, and J. R. Matarese, "Three-dimensional simulation of a magnitude 7.75 earthquake on the San Andreas fault in southern California," *Science* **270**, 1628 (1995).
3. Working Group on California Earthquake Probabilities, *Bull. Seism. Soc. Am.* **95**, 379 (1995).
4. K. B. Olsen, R. Madariaga, and R. J. Archuleta, "Three-Dimensional Dynamic Simulation of the 1992 Landers Earthquake," *Science* **278**, 834 (1997).
5. R. A. Harris, R. J. Archuleta, and S. M. Day, "Fault steps and the dynamic rupture process: 2-D numerical simulations of a spontaneously propagating shear fracture," *Geophys. Res. Lett.* **18**, 893 (1991).
6. R. A. Harris and S. M. Day, "Dynamics of fault interaction: Parallel strike slip faults," *J. Geophys. Res.* **98**, 4461 (1993).
7. D. J. Wald and T. H. Heaton, "Spatial and temporal distribution of slip for the 28 June 1998 Landers, California, earthquake," *Bull. Seism. Soc. Am.* **84**, 668 (1994).

8. J. N. Brune, "Earthquake physics, precarious rocks, and underestimates and overestimates of strong ground motion," *EOS Trans. AGU* **79**, F624 (1998).
9. A. Frankel, C. Mueller, T. Barnhard, D. Perkins, E. V. Leyendecker, N. Dickman, S. Hanson, and M. Hopper, "National seismic hazard maps," June 1996, U.S. Department of the Interior, U.S. Geological Survey (1996).
10. H. Magistrale, R. Graves, and R. Clayton, "A standard three-dimensional seismic velocity model for southern California: Version 1," *EOS Trans. AGU* **79**, F605 (1998).
11. D. Hadley and H. Kanamori, "Seismic structure of the Transverse Ranges, California," *Geol. Soc. Am. Bull.* **88**, 1469 (1977).
12. L. Y. Faust, "Seismic velocity as a function of depth and geologic time," *Geophysics* **16**, 192 (1951).
13. J. E. Nafe and C. L. Drake, "Physical properties of marine sediments," in *The Sea 3*, ed. M. N. Hill (Interscience, New York, 1960), pp. 794–815.
14. W. J. Ludwig, J. E. Nafe, and C. L. Drake, "Seismic refraction," in *The Sea 4*, ed. A. E. Maxwell (Wiley-Interscience, New York, 1970), pp. 53–84.
15. K. B. Olsen, "Simulation of three-dimensional wave propagation in the Salt Lake Basin," Ph.D. Thesis, University of Utah, Salt Lake City, Utah, 1994.
16. K. B. Olsen and R. J. Archuleta, "Three-dimensional simulation of earthquakes on the Los Angeles Fault System," *Bull. Seism. Soc. Am.* **86**, 575 (1996).
17. K. B. Olsen, "Site amplification in the Los Angeles basin from 3D modeling of ground motion," *Bull. Seism. Soc. Am.* **90**, S77 (2000).
18. R. W. Graves, "Simulating seismic wave propagation in 3D elastic media using staggered-grid finite-differences," *Bull. Seism. Soc. Am.* **86**, 1091 (1996).
19. A. R. Levander, "Fourth-order finite-difference P-SV seismograms," *Geophysics* **53**, 1425 (1988).
20. R. Clayton and B. Engquist, "Absorbing boundary conditions for acoustic and elastic wave equations," *Bull. Seism. Soc. Am.* **67**, 1529 (1977).
21. C. Cerjan, D. Kosloff, R. Kosloff, and M. Reshef, "A nonreflecting boundary condition for discrete acoustic and elastic wave equations," *Geophysics* **50**, 705 (1985).
22. J. O. A. Robertsson, J. O. Blanch, and W. W. Symes, "Viscoelastic finite-difference modeling," *Geophysics* **59**, 1444 (1994).
23. J. O. Blanch, J. O. A. Robertsson, and W. W. Symes, "Modeling of a constant Q: methodology and algorithm for an efficient and optimally inexpensive viscoelastic technique," *Geophysics* **60**, 176 (1995).
24. S. Peyrat, K. B. Olsen, and R. Madariaga, "Dynamic modeling of the 1992 Landers earthquake," *Jour. Geophys. Res.*, in press.
25. K. B. Olsen, J. C. Pechmann, and G. T. Schuster, "Simulation of 3-D elastic wave propagation in the Salt Lake Basin," *Bull. Seism. Soc. Am.* **85**, 1688 (1995).